Check for updates

Tunable magnetic ground states of iron monolayer on nonmagnetic metallic substrates by small in-plane strains

Ling Tan, Lei Wang [ID] * and Tai Min [ID]

The magnetic states of one single atomic layer of iron epitaxially grown on 4d and 5d nonmagnetic metals are studied under strain systematically using first principle calculations. Our results show that, without strain, the iron on top of different 4d and 5d nonmagnetic metals shows distinct antiferromagnetic or ferromagnetic ground states: a parallel antiferromagnetic ground state (p-AFM) on Rh and a central antiferromagnetic ground state (c-AFM) on Ir and ferromagnetic (FM) ground state on Pd, Ag, Pt and Au. However, when introducing in-plane biaxial and uniaxial strain ($\Delta\varepsilon_{xx}$) on the substrates, the ground state of iron can be manipulated easily. In detail, for biaxial strain, the ground state of iron on an Rh substrate becomes FM when $\Delta\varepsilon_{xx} < -2.0\%$ and c-AFM when $\Delta\varepsilon_{xx} > 0.8\%$, and on an Ir substrate, the ground state of iron becomes FM when $\Delta\varepsilon_{xx} < -2.8\%$ and c-AFM when $\Delta\varepsilon_{xx} > -0.8\%$. However, for the uniaxial strain along the x direction, while using the corresponding Poisson's ratios to determine the strain along the y direction, the ground state of iron on an Rh substrate remains the p-AFM state, but on an Ir substrate, the ground state of iron changes from c-AFM to p-AFM at $\Delta\varepsilon_{xx} = 0.2\%$ or $\Delta\varepsilon_{xx} = -0.3\%$ along the x direction respectively.

1 Introduction

Magnetism of low dimensional materials has been studied over the years, and is now becoming much more attractive as two dimensional magnetic materials were found to exist in recent years.[1–5] Interfaces/surfaces of metallic thin films are some of the typical low dimensional materials, and the corresponding magnetism has been proved to be tunable by electric field, significantly,[6–11] which makes them more advantageous in spin transfer torque magnetic random access memory (STT-MRAM) applications.[12,13]

However, during the past two decades, theoretical and experimental investigations have already been performed to study the magnetism of ultra-thin magnetic films or even a single magnetic monolayer on nonmagnetic substrates,[14–23] in which the magnetic states are found to be strongly dependent on substrates[24–27] and interface distance.[28,29] Moreover, when introduce the spin–orbit interaction (SOI), the non-collinear contribution from Dzyaloshinskii–Moriya interaction (DMI) induced by broken inversion symmetry could make the magnetic order more complicated.[30,31] For example, a long period (~12 nm) spin spiral state has been found in the monolayer Mn on the W substrate[32] and an 120° Néel structure in Fe on Re or Ru substrates together with an unexpected double-row-wise AFM structure on Rh substrate has been reported respectively.[27]

The adsorption of light atoms on magnetic surfaces when preparing the samples, such as oxygen and hydrogen, are also important for the magnetic ground state. In detail, a possible residual hydrogen contamination has been reported to have weak effect on the interface distances of Fe/Ir bilayer system.[29] And the adsorption of oxygen was proved to be able to significantly increases the Fe/Ir distance, which led to a p-AFM ground state.[33] Also, for the same Fe/Ir system, with half monolayer oxygen coverage of the magnetic film, DMI was sufficiently strong to stabilize a right-rotating cycloidal spin-spiral state.[34]

All the above discoveries indicate that the interfaces are the key of the magnetic order in bilayer systems. In this paper, we study the magnetic ground states for a single iron atomic layer epitaxially grown on different 4d, 5d metallic substrates and its dependence on in-plane strain. With first principle calculations, we find that, the ground state of the iron layer can change between p-AFM and c-AFM state with different strain value. The paper is structured as follows: Sec. 2 describes the computational details of our calculations. In Sec. 3 we show our results and discussion for the calculations with and without strain respectively, where we introduce both biaxial and uniaxial strain for different kinds of applications. And then, a brief conclusion is shown in Sec. 4.

Center for Spintronics and Quantum Systems, State Key Laboratory for Mechanical Behavior of Materials, Xi'an Jiaotong University, Xi'an, Shaanxi 710049, China. E-mail: wanglei.icer@xjtu.edu.cn

2   Computational details

Technically, based on the density functional theory (DFT),[35,36] the Vienna *Ab initio* Simulation Package[37,38] has been used to study the magnetic ground state of one monolayer Fe epitaxially grown on 4d, 5d metallic substrates along (001) direction. And all the calculations in this work are carried out with the projector-augmented-wave (PAW)[39,40] together with the generalized gradient approximation (GGA).[41–44] The cut-off energy for the basis is 500 eV, and the convergence criterion for the electron density self-consistency cycles is 10^{-6} eV per atom. In the Brillouin zone, we have sampled $(7 \times 7 \times 1)$ k-point grids using the Monkhorst–Pack scheme[45] to make sure the results converged. The SOI is explicitly included in our calculations, and therefore, we switch off the symmetry in all calculation.

2.1   Structural relaxation

As shown in Fig. 1, we construct the calculated geometry with one atomic layer of Fe and six atomic layers of non magnetic metals. And we insert about 20 Å vacuum layer in (001) direction to break the interaction induced by the periodic boundary condition along z direction.

To obtain the most stable structure, we first calculated the total energy of Fe/Ir for three typical cases as shown in the right panel of Fig. 1, in which, the Fe atom was put on the hollow, bridge and top position of the substrates, respectively. It can be seen that, the Hollow case has the lowest total energy, which should be much easier to be exist in experiments. And then, we focus on the hollow case and do full relaxation along x, y and z directions with a $2 \times 2 \times 1$ supercell of that in Fig. 1 to test the stableness of the Hollow case, in which the in-plane

displacement of Fe atom is found to be smaller than 10^{-6} Å. Thus, the Hollow position is already accurate enough for the in-plane relaxation. In this sense, we can just use the hollow case for all calculations and relax the distance between each atomic layer with a single unit cell of that in Fig. 1 for simple and saving computing time.

In addition, we fixed three atomic NM layers of the bottom to simulate a well grown bulk substrate and only did the relaxation inside the Fe layer and three closed NM layers. The minimal forces between the relaxed layers was set to be 1.0×10^{-4} eV Å^{-1}.

2.2   Magnetic configurations

In order to investigate the ground state of single atomic Fe layer on different substrates, we have generated four typical collinear magnetic orders using a $2 \times 2 \times 1$ supercell, as shown in Fig. 2. And they are marked as FM, p(2 × 1)-AFM, c(2 × 2)-AFM and p(1 × 2)-AFM respectively. Here one should notice that, because the x and y axis are symmetric in the case of biaxial strain and without strain, the p(2 × 1)-AFM and p(1 × 2)-AFM magnetic configurations are equivalent.

In this sense, we can calculate the energy difference ΔE between different magnetic configurations as follows:

$$\Delta E = \frac{[E(\text{AFM}) - E(\text{FM})]}{4} \tag{1}$$

and due to there are four Fe atoms in the calculations, the ΔE is divided by 4 for convenient. Then, we can define the ground state by the sign of ΔE from different magnetic configurations.

2.3   Strain effect

Strain is inevitable in the material growth process and tunable using external operations. And the strain effect in the thin films could cause lattice mismatch, defects, or even structural phase transition, which end up with the change of the electronic properties of the material. For example, Hwang *et al.*[24] reported
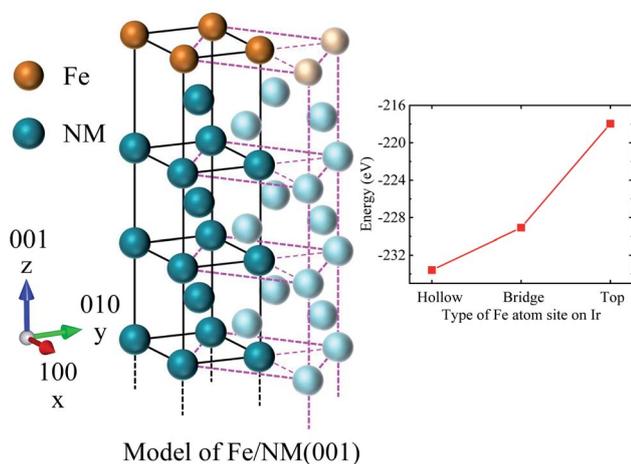

Fig. 1 The sketch of the calculated structure, where NM stand for the non magnetic metal substrates constructed by the rotated fcc structure of Rh, Pd, Ag, Ir, Pt, Au, and the dash lines are for the original view of the fcc structure. And generally, there are three typical sites for Fe on substrates, which are hollow, bridge and top, representing the Fe atom on the top of the center, edge and lattice point of the substrates, respectively. The right panel gives the calculated total energy of the three typical structures for Ir substrate, and the results confirm the ground state of the hollow case.
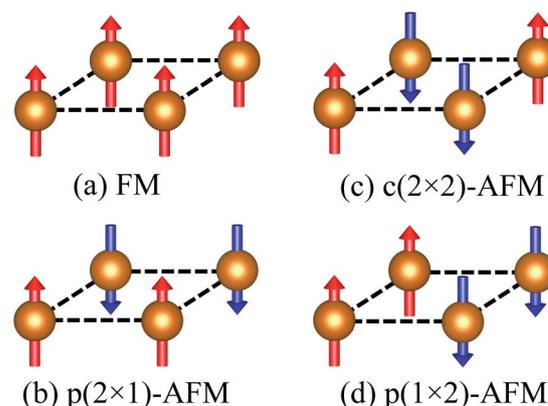

Fig. 2 Magnetic configurations of the four Fe atoms. (a) is the normal FM configuration. (b) and (d) are the parallel antiferromagnetic configurations along x and y axis respectively. Here column-wise p(1 × 2)-AFM and row-wise p(2 × 1)-AFM could be equivalent if the in-plane lattice constants along x and y axis are the same. (c) Represent central antiferromagnetic configuration c(2 × 2)-AFM.

that, the Fe could be a fcc structure when grown on a fcc substrate with a 3.6 Å lattice spacing and expected to be a bcc lattice when the lattice spacing of the fcc substrate was 4.06 Å. Therefore, researchers controlled the cooling rate, growth rate, and suitable substrate to enhance or avoid strain in the material growth process to investigate various physical phenomena.[42–44,46] For example, Shimada et al.[43] found that the Fe (001) surface appears structural and magnetic phase transition from a normal FM-bcc state to a double-layer-antiferromagnetic-fcc state under a in-plane biaxial compressive strain of $\Delta\varepsilon = 9\%$. And they also reported a magnetic phase transition from collinear FM to noncollinear spin spiral state in an Fe monolayer under a in-plane strain.[46] Thus it is very important for us to introduce different strain effect to investigate the magnetic ground states of the Fe layer on different substrates in this work.

To systematically investigate the effect of in-plane strain, we applied biaxial strain ($\Delta\varepsilon_{xx} = \Delta\varepsilon_{yy}$) and uniaxial strain ($\Delta\varepsilon_{xx} \neq \Delta\varepsilon_{yy}$) on the 4d and 5d substrates respectively. In detail, we modified the in-plane lattice constant to simulate the biaxial strain in our calculations and for uniaxial strain case, we altered the constant along x-axis with defined values $\Delta\varepsilon_{xx}$ and calculated the corresponding changes along y-axis by $\Delta\varepsilon_{yy} = \nu\Delta\varepsilon_{xx}$ according to their own Poisson's ratio ν. One should notice that, with the above strain effect, we also did the same structural relaxation as mentioned previously for all calculations.

2.4 Heisenberg exchange interaction

The Heisenberg exchange interaction is quite important for spin configurations, reads,

$$E_{tot} = E_0 - \frac{1}{2}\sum_{i,j} J_{ij} \boldsymbol{S}_i \cdot \boldsymbol{S}_j, \qquad (2)$$

where E_0 is the total energy without spin–spin interactions, J_{ij} denotes the coefficients of the Heisenberg exchange interaction between the ith and jth atoms and $\boldsymbol{S}_i$ is the corresponding spin vector of ith magnetic atom, the factor 1/2 is from double counting in the whole system.

By calculating the total energy of different magnetic configurations as shown in Sec. 2.2, we can get a set of linear equations[47,48] as listed in Table 1 to solve out the J_{ij} for further analysis. The Heisenberg exchange coefficients of the two neighbored spins coupled along the x and y axis are labeled as J_1

and J_3 respectively, and the next neighbored spins (diagonal sites) is labeled as J_2. Here, one may notice that $J_1 = J_3$ for biaxial strain cases.

3 Results and discussion

3.1 Without strain

Before things becoming too much complicated, we first studied the magnetic ground states for Fe monolayer on different substrates without strain. As mentioned previously, the three bottom layers of the substrates are fixed with their own lattice constants for the bulk limitation of the substrates, therefore, we chose the corresponding lattice constants from experimental measurements as that: $a_{Rh} = 3.8044$ Å, $a_{Pd} = 3.8907$ Å, $a_{Ag} = 4.0857$ Å, $a_{Ir} = 3.8389$ Å, $a_{Pt} = 3.9239$ Å, $a_{Au} = 4.0783$ Å.[49–54] The calculated energy differences from eqn (1) with and without SOI for all six substrates are plotted in Fig. 3, where ΔE_1 were calculated for p(2 × 1)-AFM and ΔE_2 for c(2 × 2)-AFM respectively.

From Fig. 3, we confirm that, with SOI, the magnetic ground state of Fe monolayer is c(2 × 2)-AFM state ($\Delta E_2 < \Delta E_1$) for Ir substrate.[34] However, for Rh substrate, our results show that the magnetic ground state is p(2 × 1)-AFM instead of c(2 × 2)-AFM, as shown in Fig. 3 ($\Delta E_1 < \Delta E_2$), and we also confirm that the total energy of c(2 × 2)-AFM state is lower than the FM state which is the same as ref. 55. For Pd,[14] Ag,[14] Pt and Au substrates, the magnetic ground states of Fe are all FM state. In addition, comparing the results with and without SOI, we find that the SOI does affect the detail values of the energy differences. Therefore, only the calculations with SOI are concerned in the following results.
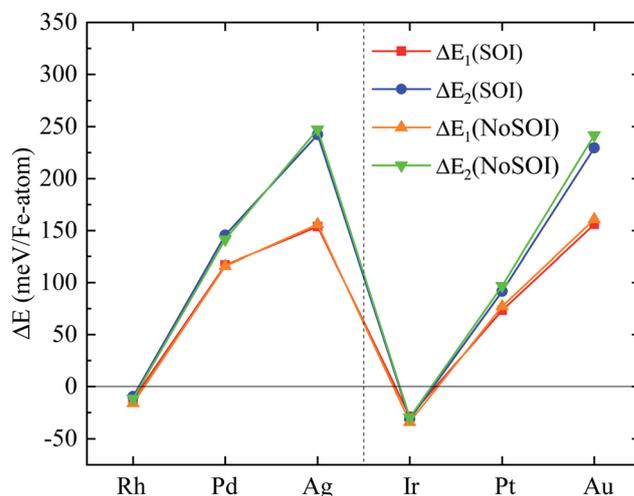

Fig. 3 The energy differences between different AFM configurations and FM state of Fe monolayer on all six substrates. And as p(2 × 1)-AFM and p(1 × 2)-AFM are equivalent without strain, we only chose p(2 × 1)-AFM and c(2 × 2)-AFM states for the calculations of eqn (1). Here ΔE_1 is for (2 × 1)-AFM, ΔE_2 is for c(2 × 2)-AFM, "SOI" and "NoSOI" represent the calculations with and without SOI respectively. Thus, a positive ΔE indicates a FM ground state, while a negative ΔE denotes different AFM orders referring to the value of ΔE_1 and ΔE_2.

Table 1 Total energies for different magnetic configurations in biaxial and uniaxial strain systems. (a, b, c and d) Represent the magnetic configurations as shown in Fig. 2, which are FM, p(2 × 1)-AFM, c(2 × 2)-AFM and p(2 × 1)-AFM respectively

Label	E_{tot} (biaxial strain)	E_{tot} (uniaxial strain)
a	$E_0 - 8J_1 - 8J_2$	$E_0 - 4J_1 - 8J_2 - 4J_3$
b	$E_0 + 8J_2$	$E_0 - 4J_1 + 8J_2 + 4J_3$
c	$E_0 + 8J_1 - 8J_2$	$E_0 + 4J_1 - 8J_2 + 4J_3$
d	—	$E_0 + 4J_1 + 8J_2 - 4J_3$

To understand the effects of substrates, we also calculated the freestanding Fe monolayer with biaxial in-plane strain from -8% to 8% and estimated the nearest neighbor Heisenberg exchange (J_1) for Fe as shown in Fig. 4. The black squares are results of Fe monolayer without substrates, while the red circles are the Fe monolayer with different substrates as labeled by the dot lines. It can be found that, for the freestanding monolayer Fe (black squares), J_1 decreases near linearly when the distance of Fe atom increases. In this sense, we can simply use a linear fitting to get the rate of change of J_1 as 80 meV Å^{-1}. At the same time, we obtained J_1 for Fe on Rh, Ir, Pd, Pt, Au and Ag substrate as -2.8 meV, -9.8 meV, 36.4 meV, 22.9 meV, 57.4 meV and 60.6 meV respectively, which means that we should change the in-plane lattice (strain) at least about 0.035 Å ($\Delta\varepsilon_{xx} = 0.9\%$) for Rh, 0.122 Å ($\Delta\varepsilon_{xx} = 3.2\%$) for Ir, 0.455 Å ($\Delta\varepsilon_{xx} = 11.7\%$) for Pd, 0.286 Å ($\Delta\varepsilon_{xx} = 7.3\%$) for Pt, 0.718 Å ($\Delta\varepsilon_{xx} = 17.6\%$) for Au and 0.757 Å ($\Delta\varepsilon_{xx} = 18.5\%$) for Ag respectively, to change the sign of J_1 for the phase transition. Therefore, if we want to tune the magnetic ground state of the Fe on Pt, Pd, Au and Ag, the strain needed will be too large to be realized and used in applications. However, for Rh and Ir substrates, J_1 is significantly reduced due to the band-filling and hybridization around the interfaces, which makes it possible to manipulate their magnetic ground states. Therefore, we will focus on Rh and Ir substrates in the rest of the paper.

3.2 Biaxial strain

The biaxial in-plane strain is simpler as that, $\Delta\varepsilon_{xx} = \Delta\varepsilon_{yy}$ and p(2 × 1)-AFM is equivalent with p(1 × 2)-AFM. Thus, we tuned the in-plane lattice constant to realize the in-plane strain from -3%

to 2% for Rh and Ir substrates, respectively. The corresponding total energies are shown in Fig. 5(a) and (c) with legends E_1, E_2 and E_3 for FM, p(2 × 1)-AFM and c(2 × 2)-AFM magnetic configurations, respectively. Moreover, the Heisenberg exchange coefficients are obtained as described in Sec. 2.4 using the calculated total energies, and the results are plotted in Fig. 5(b) and (d). And also, we used different background colors together with the insets of magnetic configurations to distinguish the different ground states by the minimum value of E_i, i $\in \{1, 2, 3\}$.

From Fig. 5(a) and (c), it can be seen that, for Rh substrate, the ground state changes from p(2 × 1)-AFM state to a FM state under a $\Delta\varepsilon_{xx} \approx -2\%$ strain and to a c(2 × 2)-AFM state under $\Delta\varepsilon_{xx} \approx 0.8\%$ strain. However, much larger compression up to -2.8% should be introduced for Ir substrate case to realize the transition from FM to p(2 × 1)-AFM and a lighter compression of -0.8% strain to transfer the states between p(2 × 1)-AFM and c(2 × 2)-AFM. Moreover, with the in-plane strain, the total energies first decrease to an optimal value of $\Delta\varepsilon_{xx}$ and then increase afterward for all lines in Fig. 5(a) and (c), which is quite similar to the lattice constant relaxation process. And moreover, the optimal in-plane lattice constant could be slightly different for different magnetic configurations, which can be treated as the inverse effect of the above strain induced magnetic phase transition.

And to understand such strain induced magnetic phase transition, we introduced the Heisenberg model. As we know, when $J_1 > 0$, the two neighbored spins along the x-axis are forced to be parallel, while when $J_1 < 0$, the two spins will be anti-parallel. And with the larger absolute value of J_1, there will be stronger force between neighbored spins. J_2 and J_3 show similar features. In this sense, from Fig. 5(b), we can see, for Rh substrate, at about -3.0%, J_2 is almost zero, and the positive J_1 determines the FM ground state. With increasing of the $\Delta\varepsilon_{xx}$, J_1 and J_2 both decrease, and until about -2%, the contributions from J_1 and J_2 are even. After that, the contribution of J_2 finally overcome that from J_1 and forces the diagonal spins to be anti-parallel. Therefore, half of the spin along x or y axis will be reversed to reduce the total energy of the system, and the ground state then drop to p(2 × 1)-AFM state.

Further more, J_1 become negative when $\Delta\varepsilon_{xx} \gtrsim -1\%$, but it is still not strong enough to overcome the contribution from J_2, so that, the ground state remains p(2 × 1)-AFM until $\Delta\varepsilon_{xx} \simeq 0.8\%$. And then, it is obvious that, when $\Delta\varepsilon_{xx} > 0.8\%$, the larger J_1 dominates and forces the neighbored spins to be anti-parallel, which end up with the c(2 × 2)-AFM ground state. Similar explanation can be used to understand what happened for Ir substrate as shown in Fig. 5(d). And for both Rh and Ir substrates, there appear three typical magnetic ground states due to the crossing of strain dependent J_1 and J_2.
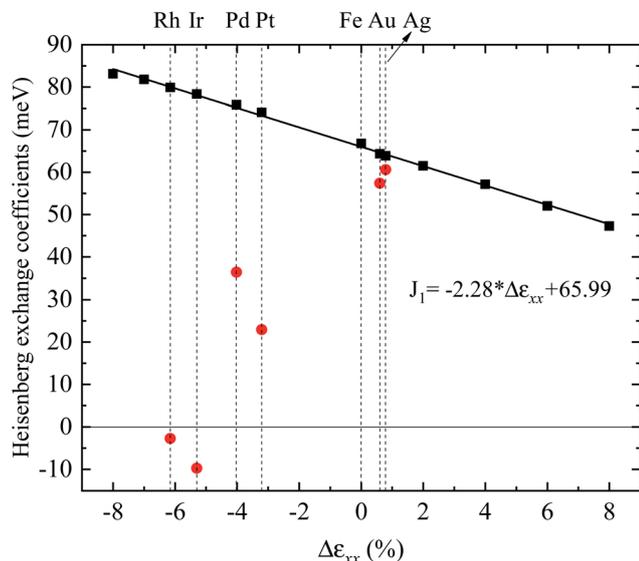

Fig. 4 The nearest neighbor Heisenberg exchange coefficients J_1 of the freestanding Fe monolayer (black squares) and the same results with different substrates (red cycles), obtained using the total energies as described in Sec. 2.4. Here one may notice that, as we rotate 45° of bcc Fe to match the fcc substrates, the lattice constant of Fe is scaled by a factor of $\sqrt{2}$ for comparison. And a positive J_1 indicates FM coupling, while a negative J_1 denotes AFM coupling.

3.3 Uniaxial strain

Similarly, we investigated the magnetic ground states of Fe monolayer on Rh and Ir substrates with uniaxial strain $\Delta\varepsilon_{xx}$ from -1% to 1%. However, as $\Delta\varepsilon_{xx} \neq \Delta\varepsilon_{yy}$ in this case, p(2 × 1)-AFM and p(1 × 2)-AFM states are no longer equivalent. And the
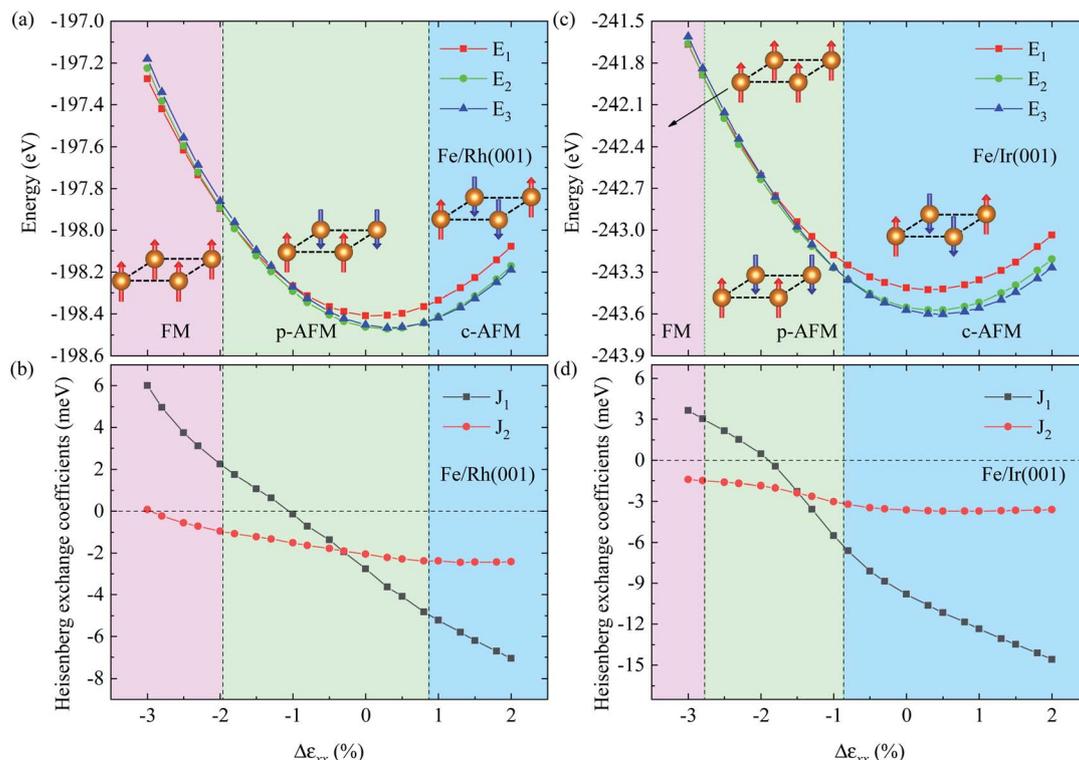
Fig. 5 The total energies with varying biaxial strain from −3% to 2% for Rh (a) and Ir (c) substrates, respectively. (b and d) Plot the corresponding Heisenberg exchange coefficients obtained using the total energies as described in Sec. 2.4. The total energies of FM state are with legend E_1, and E_2 for p(2 × 1)-AFM state, E_3 for c(2 × 2)-AFM state. The background colors represent the corresponding magnetic ground state determined by the minimum value of E_i, $i \in \{1, 2, 3\}$.

$\Delta \varepsilon_{yy}$ is determined by the defined $\Delta \varepsilon_{xx}$ and their own Poisson's ratios ν, which are $\nu_{Rh} = 0.32$ and $\nu_{Ir} = 0.26$ for Rh and Ir respectively.[56] Therefore, we calculated four probable magnetic configurations as shown in Fig. 2, and we used an extra legend E_4 for the new p(1 × 2)-AFM state together with the same E_i, $i \in \{1, 2, 3\}$ as shown in Fig. 5. And the background colors are the corresponding magnetic ground states, *i.e.* the light green is for p(2 × 1)-AFM, light blue is for c(2 × 2)-AFM and light purple is for p(1 × 2)-AFM.

Different with the biaxial strain, there only exist two magnetic ground states for Rh substrate as shown in Fig. 6(a), and the boundary of p(2 × 1)-AFM and p(1 × 2)-AFM is 0%. However, if we neglect the asymmetry from Poisson's ratio, p(2 × 1)-AFM and p(1 × 2)-AFM states are still the same with 90° rotation. In this sense, the p-AFM state is quite robust under uniaxial strain. And with the Heisenberg exchange coefficients shown in Fig. 6(b), it can be seen that, J_2 is almost constant with varying $\Delta \varepsilon_{xx}$, which is the key of the stable p-AFM ground state.

While for Ir substrate as shown in Fig. 6(c), the transition from p(2 × 1) to c(2 × 2)-AFM appears at $\Delta \varepsilon_{xx} \approx -0.3\%$ and from c(2 × 2) to p(1 × 2)-AFM at $\Delta \varepsilon_{xx} \approx 0.2\%$. We can also analysis this phenomenon by strain dependent Heisenberg exchange coefficients as shown in Fig. 6(d). Similarly, as described in biaxial strain, the neighbored spins along the x- and y-axis favor FM state if $J_1 > 0$ and $J_3 > 0$, and if $J_2 < 0$ at the same time, the p(2 × 1)-AFM and p(1 × 2)-AFM could exist. That

is why we have p-AFM state in a broaden region, and when J_1 and J_3 are both strong enough to overcome the contribution from J_2, the magnetic ground state becomes c(2 × 2)-AFM.

3.4 Phase diagrams

For a clear view of the magnetic ground state of the Fe monolayer on Rh and Ir substrates. We calculated the total energies of the four typical magnetic configurations as shown in Sec. 2.2 with only defined Heisenberg exchange coefficients J_i, $i \in \{1, 2, 3\}$, and found the magnetic ground states by the calculated minimum total energies. The corresponding phase diagrams are plotted in Fig. 7(a) and (b) for biaxial and uniaxial train respectively, where we used different colors to represent different magnetic ground states. Also, we plotted the J_i, $i \in \{1, 2, 3\}$ from the previous first principle calculations into Fig. 7 with solid cycles for detail comparison, where black cycles were from Rh substrate and blue cycles were from Ir substrate. It can be seen that, the magnetic ground states from first principle calculations are perfect consistent with the results from direct Heisenberg exchange coefficients.

And moreover, we can see that, from Fig. 7(a), there will appear three typical magnetic ground states with a negative J_2 when varying J_1, but only c(2 × 2)-AFM and FM states with a positive J_2. These phenomena agree with the calculated results in Fig. 5, where J_2 remains negative for both Rh and Ir substrates in a broaden region of biaxial strain. Also, from
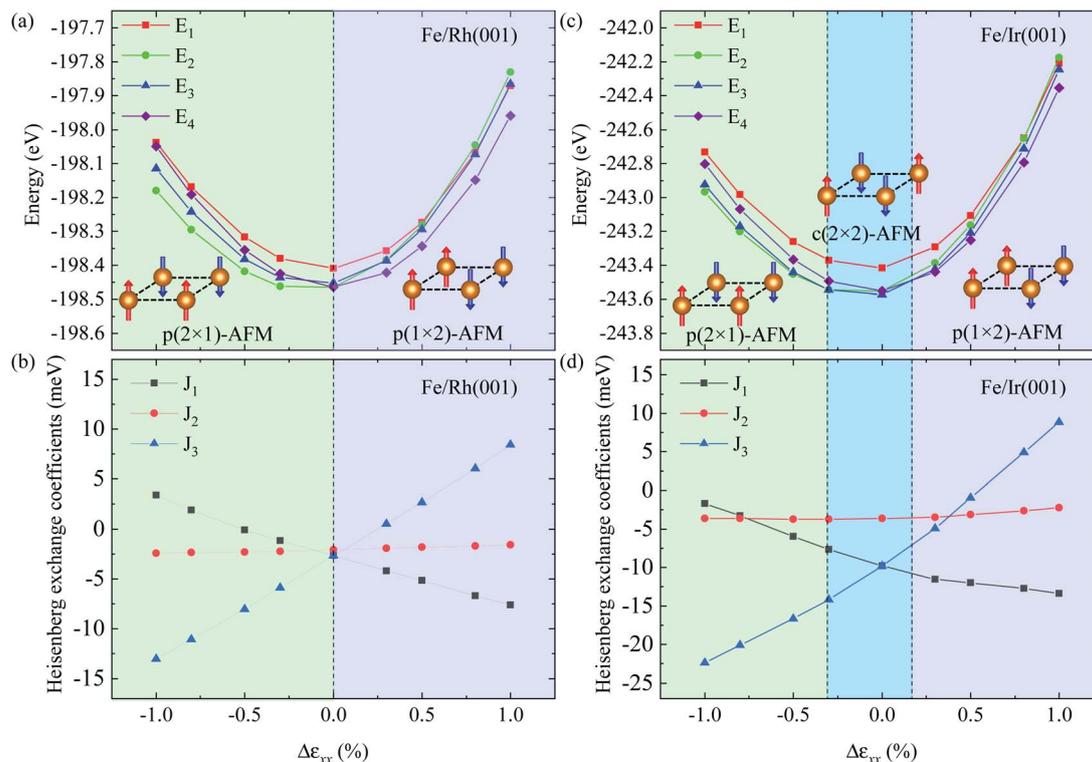
Fig. 6 The total energies with varying uniaxial strain from −1% to 1% for Rh (a) and Ir (c) substrates, respectively. (b and d) Plot the corresponding Heisenberg exchange coefficients obtained using the total energies as described in Sec. 2.4. The legends of the total energies are the same with that in Fig. 5 with an extra E_4 for the p(1×2)-AFM state. The background colors represent the corresponding magnetic ground state determined by the minimum value of E_i, $i \in \{1, 2, 3, 4\}$.

Fig. 7(b), due to the large negative J_1 and J_3 for Ir substrate, the blue cycles pass through the c-AFM region, but black cycles do not. This is why there are only two magnetic ground states for Rh substrate, but three for Ir substrate as shown in Fig. 6. In this sense, both the nearest neighbored Heisenberg exchange

coefficients $J_{1/3}$ and the next neighbored Heisenberg exchange coefficient J_2 are important to tune the magnetic ground state of the Fe monolayer on Rh or Ir substrates.

3.5 Discussion

In the first principle calculations, the choosing of GGA, LDA, *etc.* will affect slightly the optimal lattice constant of materials. In this sense, the zero point of strain ($\Delta \varepsilon_{xx} = 0$) in our calculations using the experimental lattice constant is the same as that using the calculated lattice constant with finite strain. This effect can be considered as a renormalization of $\Delta \varepsilon_{xx}$ in Fig. 5 and 6 without changing anything else. Therefore, only the phase transition points are shifted within a small value, our main point of the strain induced magnetic phase transitions will still be valid.

However, as the experimental measurement is practical when one grows a thin film, we chose the experimental lattice constant as described previously to make our results suitable for future experimental confirmations and chose GGA due to its accurately reproduce the structural and magnetic ground state.[41–44]
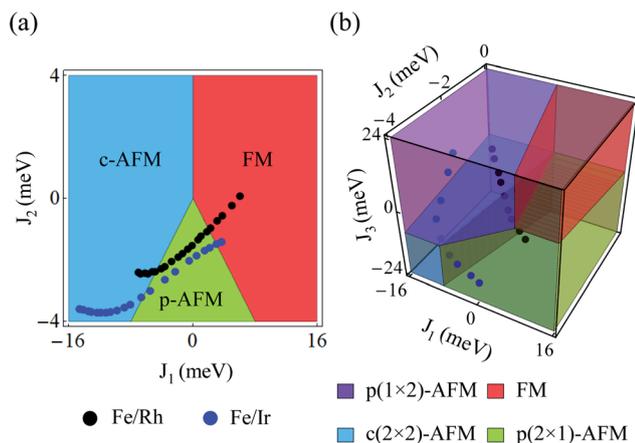

Fig. 7 The phase diagrams of the magnetic ground states for both biaxial (a) and uniaxial (b) strain. Here the red, green, blue and purple colors filled in diagrams indicate the FM, p(2×1)-AFM, c(2×2)-AFM and p(1×2)-AFM ground states, respectively. The solid cycles are all obtain from Fig. 5(b), (d) and 6(b), (d), where black cycles are from Rh substrate and blue cycles from Ir substrate.

4   Conclusions

We studied the magnetic ground states for the Fe monolayer on 4d, 5d non-magnetic metallic substrates using first-principles

calculations. Without in-plane strain, we observed p-AFM ground state of Fe monolayer on Rh substrate and c-AFM on Ir substrate, while FM ground state on the rest of other four substrates. Furthermore, we observed magnetic phase transitions for both Rh and Ir substrates under small in-plane strain. In detail, for Rh substrate, with biaxial strain, the phase transition from FM to p(2 × 1)-AFM appears at about −2% and from p(2 × 1) to c(2 × 2)-AFM at about 0.8%; with uniaxial strain, the phase transition from p(2 × 1)-AFM to p(1 × 2)-AFM at 0%. For Ir substrate, with biaxial strain, the phase transitions from FM to p(2 × 1)-AFM appears at about −2.8% and from p(2 × 1)-AFM to c(2 × 2)-AFM at about −0.8%; with uniaxial strain, the phase transition from p(2 × 1) to c(2 × 2)-AFM at −0.3% and from c(2 × 2)-AFM to p(1 × 2)-AFM at 0.2%. Moreover, we used the Heisenberg model to explain the above discoveries, and showed the relations between the magnetic ground states and the Heisenberg exchange coefficients by phase diagrams.

Conflicts of interest

There are no conflicts of interest to declare.

Acknowledgements

Notes and references

1 Y. Deng, Y. Yu, Y. Song, J. Zhang, N. Z. Wang, Y. Z. Wu, J. Zhu, J. Wang, X. H. Chen and Y. Zhang, *Nature*, 2018, 1–17.

2 B. Huang, G. Clark, D. R. Klein, D. MacNeill, E. Navarro-Moratalla, K. L. Seyler, N. Wilson, M. A. McGuire, D. H. Cobden, D. Xiao, W. Yao, P. Jarillo-Herrero and X. Xu, *Nat. Nanotechnol.*, 2018, **13**, 544–548.

3 Z. Fei, W. Zhao, T. A. Palomaki, B. Sun, M. K. Miller, Z. Zhao, J. Yan, X. Xu and D. H. Cobden, *Nature*, 2018, **560**, 336–339.

4 E. Vatansever, S. Sarikurt, F. Ersan, Y. Kadioglu, O. Ü. Aktürk, Y. Yüksel, C. Ataca, E. Aktürk and Ü. Akıncı, *J. Appl. Phys.*, 2019, **125**, 083903.

5 F. Ersan, E. Vatansever, S. Sarikurt, Y. Yüksel, Y. Kadioglu, H. D. Ozaydin, O. Ü. Aktürk, Ü. Akıncı and E. Aktürk, *J. Magn. Magn. Mater.*, 2019, **476**, 111–119.

6 Q. Yang, L. Wang, Z. Zhou, L. Wang, Y. Zhang, S. Zhao, G. Dong, Y. Cheng, T. Min, Z. Hu, W. Chen, K. Xia and M. Liu, *Nat. Commun.*, 2018, **9**, 991.

7 M. Guan, L. Wang, S. Zhao, Z. Zhou, G. Dong, W. Su, T. Min, J. Ma, Z. Hu, W. Ren, Z.-G. Ye, C.-W. Nan and M. Liu, *Adv. Mater.*, 2018, **30**, 1802902.

8 M. Guan, L. Wang, S. Zhao, B. Peng, W. Su, Z. He, G. Dong, T. Min, J. Ma, Z. Hu, W. Ren, Z.-G. Ye, C.-W. Nan, Z. Zhou and M. Liu, *Adv. Funct. Mater.*, 2019, **29**, 1805592.

9 L. Wang, X. R. Wang, T. Min and K. Xia, *Phys. Rev. B*, 2019, **99**, 224416.

10 S. Zhao, L. Wang, Z. Zhou, C. Li, G. Dong, L. Zhang, B. Peng, T. Min, Z. Hu, J. Ma, W. Ren, Z.-G. Ye, W. Chen, P. Yu, C.-W. Nan and M. Liu, *Adv. Mater.*, 2018, **30**, 1801639.

11 A. O. Leon, J. d'Albuquerque e Castro, J. C. Retamal, A. B. Cahaya and D. Altbir, *Phys. Rev. B*, 2019, **100**, 014403.

12 R. Hao, L. Wang and T. Min, *IEEE Trans. Magn.*, 2019, **55**, 1–6.

13 L. Wang, R. Hao and T. Min, arXiv:1907.09861, 2019.

14 S. Blügel, M. Weinert and P. Dederichs, *Phys. Rev. Lett.*, 1988, **60**, 1077.

15 C. Li, A. J. Freeman, H. Jansen and C. Fu, *Phys. Rev. B: Condens. Matter Mater. Phys.*, 1990, **42**, 5433.

16 J. Ortega and F. Himpsel, *Phys. Rev. B: Condens. Matter Mater. Phys.*, 1993, **47**, 16441.

17 P. Ferriani, S. Heinze, G. Bihlmayer and S. Blügel, *Phys. Rev. B: Condens. Matter Mater. Phys.*, 2005, **72**, 024452.

18 A. Kubetzka, P. Ferriani, M. Bode, S. Heinze, G. Bihlmayer, K. Von Bergmann, O. Pietzsch, S. Blügel and R. Wiesendanger, *Phys. Rev. Lett.*, 2005, **94**, 087204.

19 S. Blügel, *Phys. Rev. Lett.*, 1992, **68**, 851.

20 K. Von Bergmann, S. Heinze, M. Bode, E. Vedmedenko, G. Bihlmayer, S. Blügel and R. Wiesendanger, *Phys. Rev. Lett.*, 2006, **96**, 167203.

21 V. Martin, W. Meyer, C. Giovanardi, L. Hammer, K. Heinz, Z. Tian, D. Sander and J. Kirschner, *Phys. Rev. B: Condens. Matter Mater. Phys.*, 2007, **76**, 205418.

22 P. Ferriani, K. Von Bergmann, E. Vedmedenko, S. Heinze, M. Bode, M. Heide, G. Bihlmayer, S. Blügel and R. Wiesendanger, *Phys. Rev. Lett.*, 2008, **101**, 027201.

23 J. Kemmer, S. Wilfert, J. Kügel, T. Mauerer, P.-J. Hsu and M. Bode, *Phys. Rev. B: Condens. Matter Mater. Phys.*, 2015, **91**, 184412.

24 C. Hwang, A. Swan and S. Hong, *Phys. Rev. B: Condens. Matter Mater. Phys.*, 1999, **60**, 14429.

25 Y. Meng, K. Zakeri, A. Ernst, T.-H. Chuang, H. Qin, Y.-J. Chen and J. Kirschner, *Phys. Rev. B: Condens. Matter Mater. Phys.*, 2014, **90**, 174437.

26 P. Ferriani, I. Turek, S. Heinze, G. Bihlmayer and S. Blügel, *Phys. Rev. Lett.*, 2007, **99**, 187203.

27 B. Hardrat, A. Al-Zubi, P. Ferriani, S. Blügel, G. Bihlmayer and S. Heinze, *Phys. Rev. B: Condens. Matter Mater. Phys.*, 2009, **79**, 094411.

28 D. Spišák and J. Hafner, *Phys. Rev. B: Condens. Matter Mater. Phys.*, 2006, **73**, 155428.

29 J. Kudrnovský, F. Máca, I. Turek and J. Redinger, *Phys. Rev. B: Condens. Matter Mater. Phys.*, 2009, **80**, 064405.

30 A. Deák, L. Szunyogh and B. Ujfalussy, *Phys. Rev. B: Condens. Matter Mater. Phys.*, 2011, **84**, 224413.

31 S. Meyer, B. Dupé, P. Ferriani and S. Heinze, *Phys. Rev. B*, 2017, **96**, 094408.

32 M. Bode, M. Heide, K. Von Bergmann, P. Ferriani, S. Heinze, G. Bihlmayer, A. Kubetzka, O. Pietzsch, S. Blügel and R. Wiesendanger, *Nature*, 2007, **447**, 190.

33 F. Máca, J. Kudrnovský, V. Drchal and J. Redinger, *Phys. Rev. B: Condens. Matter Mater. Phys.*, 2013, **88**, 045423.

34 A. Belabbes, G. Bihlmayer, S. Blügel and A. Manchon, *Sci. Rep.*, 2016, **6**, 24634.

35 P. Hohenberg and W. Kohn, *Phys. Rev.*, 1964, **136**, B864.

36 W. Kohn and L. J. Sham, *Phys. Rev.*, 1965, **140**, A1133.

37 G. Kresse and J. Hafner, *Phys. Rev. B: Condens. Matter Mater. Phys.*, 1993, **47**, 558.

38 G. Kresse and J. Furthmüller, *Phys. Rev. B: Condens. Matter Mater. Phys.*, 1996, **54**, 11169.

39 P. E. Blöchl, *Phys. Rev. B: Condens. Matter Mater. Phys.*, 1994, **50**, 17953.

40 G. Kresse and D. Joubert, *Phys. Rev. B: Condens. Matter Mater. Phys.*, 1999, **59**, 1758.

41 E. Moroni, G. Kresse, J. Hafner and J. Furthmüller, *Phys. Rev. B: Condens. Matter Mater. Phys.*, 1997, **56**, 15629.

42 M. Zelený, D. Legut and M. Šob, *Phys. Rev. B: Condens. Matter Mater. Phys.*, 2008, **78**, 224105.

43 T. Shimada, Y. Ishii and T. Kitamura, *Phys. Rev. B: Condens. Matter Mater. Phys.*, 2010, **81**, 134420.

44 T. Shimada, J. Okuno, Y. Ishii and T. Kitamura, *J. Phys.: Condens. Matter*, 2012, **24**, 095303.

45 H. J. Monkhorst and J. D. Pack, *Phys. Rev. B: Condens. Matter Mater. Phys.*, 1976, **13**, 5188.

46 T. Shimada, J. Okuno and T. Kitamura, *Phys. Rev. B: Condens. Matter Mater. Phys.*, 2012, **85**, 134440.

47 C. Wang, G.-C. Guo and L. He, *Phys. Rev. B: Condens. Matter Mater. Phys.*, 2008, **77**, 134113.

48 M. Gao, X.-W. Yan and Z.-Y. Lu, *J. Phys.: Condens. Matter*, 2012, **25**, 036004.

49 I. Kornilov and K. Myasnikova, *Russ. Metall.*, 1965, 107–109.

50 I. Harris, M. Norman and A. Bryant, *J. Less-Common Met.*, 1968, **16**, 427–440.

51 M. Ellner, K. Kolatschek and B. Predel, *J. Less-Common Met.*, 1991, **170**, 171–184.

52 M. Beck, M. Ellner and E. Mittemeijer, *Acta Mater.*, 2001, **49**, 985–993.

53 B. Manoun, S. K. Saxena, H.-P. Liermann and M. W. Barsoum, *J. Am. Ceram. Soc.*, 2005, **88**, 3489–3491.

54 R. Preston, *J. Mater. Sci.*, 1966, **1**, 309–310.

55 A. Al-Zubi, G. Bihlmayer and S. Blügel, *Phys. Rev. B: Condens. Matter Mater. Phys.*, 2011, **83**, 024407.

56 http://asia.matweb.com.